

Cite this: *RSC Adv.*, 2019, 9, 21777Received 18th May 2019  
Accepted 29th June 2019

DOI: 10.1039/c9ra03755a

rsc.li/rsc-advances

# Enhanced photoelectrochemical performance of TiO<sub>2</sub> nanorod array films based on TiO<sub>2</sub> compact layers synthesized by a two-step method

Yafeng Deng,<sup>a</sup> Zhanhong Ma,<sup>a</sup> Fengzhang Ren<sup>\*ab</sup> and Guangxin Wang<sup>ac</sup>

An innovative two-step method perfectly prepared TCLs with different thicknesses, and then the TNA films based on TCLs were successfully prepared. The effects of different thicknesses of TCLs on the morphology and photoelectrochemical performance of TNA films were investigated. The results indicated that TCLs with appropriate thickness could effectively improve the morphology and photoelectrochemical performance of TNA films. Compared with the TNA films based on TCL<sub>5</sub>, TCL<sub>10</sub> and TCL<sub>30</sub>, the TNA film based on TCL<sub>20</sub> exhibited more ideal and comprehensive photoelectrochemical performance. Moreover, dye-sensitized solar cells (DSSCs) based on this TNA film achieved the highest  $J_{sc}$  (10.2054 mA cm<sup>-2</sup>),  $V_{oc}$  (0.5737 V), PCE (3.3%) and  $P_{out}$  (3.31 mW cm<sup>-2</sup>).

## Introduction

As the third-generation solar cells, non-pn junction thin film solar cells have become an important research field in the world. Its typical representatives include Perovskite solar cells (PSCs),<sup>1-4</sup> dye-sensitized solar cells (DSSCs),<sup>5-8</sup> and quantum dots-sensitized solar cells (QDSCs).<sup>9-12</sup> Among them, a huge application potential of DSSCs relies on their advantages, such as lower cost, light weight, effective use of diffuse light, better performance under weak light, and possibility to form flexible cells and to be designed double-sided or with multi-color appearance. In addition, with the in-depth study of DSSC basic theory, the performance of the cells will be further improved to become practical solar cells with low-cost and high photoelectric conversion efficiency. As the key electron transport layer material, the photoanode plays an important role in the final performance of DSSCs. Common electron transport layer materials include TiO<sub>2</sub>,<sup>13,14</sup> ZnO,<sup>15,16</sup> SnO<sub>2</sub> (ref. 17 and 18) and Nb<sub>2</sub>O<sub>5</sub>.<sup>19,20</sup> As a typical wide-band gap transition metal oxide semiconductor (MOS) material, TiO<sub>2</sub> has excellent physical and chemical properties. TiO<sub>2</sub> with its high chemical stability, appropriate band gap, good photoelectric conversion performance, excellent charge separation and transmission capacity, as well as low-price, non-toxicity and abundant

reserves, has always been the research emphasis for electron transport layer materials.<sup>21-25</sup>

As typical TiO<sub>2</sub> materials, the one-dimensional TiO<sub>2</sub> materials have been extensively studied. Currently, the main methods for the preparation of the one-dimensional TiO<sub>2</sub> nanomaterials include hydrothermal,<sup>26,27</sup> anodic oxidation<sup>28,29</sup> and template method,<sup>30</sup> among which the hydrothermal method is the most commonly used. On the one hand, the hydrothermal method can directly grow one-dimensional TiO<sub>2</sub> nanomaterials on a conductive substrate, which are firmly combined with the substrate and well oriented. On the other hand, the hydrothermal method presents the advantages, such as low-cost, short synthesis cycle, process simplicity as well as easy realization and regulation of reaction conditions. As the electron transport layer materials, the one-dimensional TiO<sub>2</sub> nanomaterials can not only reduce the band edge, surface state and crystal defects but also effectively enhance the light-scattering effect of the photoanode.<sup>31-35</sup> Moreover, the one-dimensional nanomaterials provide a nearly linear transmission path for electrons, which greatly shortens the electron transport distance, prolongs the electron lifetime, reduces the charge recombination, thereby improving the carrier quantum yield and laying a foundation for the good photoelectric performance of solar cells.<sup>36,37</sup> However, the nucleation type of TiO<sub>2</sub> nanorods formed on the bare FTO substrate is a primary nucleation, in which the system does not contain substances to be crystallized. There is a certain lattice mismatch between the TiO<sub>2</sub> crystal and the SnO<sub>2</sub> crystal in the substrate. Thus, to crystallize TiO<sub>2</sub> on the FTO substrate it has to overcome the large energy barrier caused by the lattice mismatch, which adversely affects the crystal growth of TiO<sub>2</sub> nanorods. Moreover, the nucleation type of TiO<sub>2</sub> nanorods based on TiO<sub>2</sub> compact layers (TCLs) follows the secondary nucleation, *i.e.* the system

<sup>a</sup>School of Materials Science and Engineering, Henan University of Science and Technology, Luoyang, 471023, P. R. China. E-mail: dengyf1111@126.com; renfz@haust.edu.cn

<sup>b</sup>Henan Collaborative Innovation Centre of Non-Ferrous Generic Technology, Luoyang, 471023, P. R. China

<sup>c</sup>Henan Key Laboratory of Non-Ferrous Materials Science & Processing Technology, Luoyang, 471023, P. R. China

contains substances to be crystallized at the time of nucleation. Since there is no lattice mismatch,  $\text{TiO}_2$  is more susceptible to the nucleation crystallization on TCLs and the effect of TCLs on the growth of  $\text{TiO}_2$  crystal will eventually have a certain impact on the photoelectrochemical performance of  $\text{TiO}_2$  nanorods.<sup>38–40</sup>

Herein, the innovative two-step method was used to prepare perfect TCLs with different thicknesses. The FTO substrate with TCL was named as  $\text{FTO}_{\text{TCL}}$ . In previous studies, TCLs were mostly synthesized by liquid phase deposition,<sup>27,41</sup> spin-coating,<sup>39,42</sup> atomic layer deposition<sup>43,44</sup> and sol-gel process.<sup>45,46</sup> However, the liquid phase deposition and atomic layer deposition have high technical operation requirements; moreover, these processes are complex and their cost is high. Spin-coating and sol-gel coating are easy to be realized, but the coating effect is poor. Therefore, we innovatively proposed a two-step method, which is simple and low-cost while guaranteeing a good film-forming effect. Completely different from the mentioned methods, in this study, the first step in preparing TCL was to deposit a nano-metal Ti compact layer on the FTO substrate by a magnetron sputtering technology, and the second step was to transform the nano-metal Ti compact layer into the required TCL by an oxidation treatment under certain conditions (the TCLs based on different magnetron sputtering times were defined as  $\text{TCL}_5$ ,  $\text{TCL}_{10}$ ,  $\text{TCL}_{20}$  and  $\text{TCL}_{30}$ ). Then, a layer of well-crystallized one-dimensional  $\text{TiO}_2$  nanorod array film (TNA film) based on the TCL was grown by the hydrothermal method as electron transport layer. The samples were characterized by field emission scanning electron microscopy (FESEM), X-ray diffraction (XRD), UV-Vis spectroscopy, photoluminescence (PL) spectroscopy, electrochemical impedance spectroscopy (EIS), Bode plots and Mott-Schottky plots. The effects of TCLs with different thicknesses prepared by changing the magnetron sputtering time on TNA films were studied. The results showed that TNA films based on the  $\text{TCL}_{20}$  obtained better and comprehensive photoelectrochemical properties, and thus the DSSCs based on this TNA film achieved the highest  $J_{\text{sc}}$  ( $10.2054 \text{ mA cm}^{-2}$ ),  $V_{\text{oc}}$  ( $0.5737 \text{ V}$ ), PCE ( $3.3\%$ ) and  $P_{\text{out}}$  ( $3.31 \text{ mW cm}^{-2}$ ).

## Experimental

### Materials

Pure titanium target ( $\phi 50 \times 4 \text{ mm}$ ,  $\geq 99.995\%$ ) was purchased from the Deyang ONA New Materials Co., Ltd. F-doped  $\text{SnO}_2$  transparent conductive glass (FTO,  $30 \times 30 \times 2.2 \text{ mm}$ , square resistance  $\leq 7 \Omega \square^{-1}$ , transmittance  $\geq 80\%$ ) was purchased from the South China Science & Technology Co., Ltd. Tetrabutyl titanate ( $\geq 98\%$ ), titanium tetrachloride ( $\geq 98\%$ ), hydrochloric acid ( $36\text{--}38 \text{ wt}\%$ ), anhydrous ethanol ( $\geq 99.7\%$ ), acetone ( $\geq 99.5\%$ ), isopropanol ( $\geq 99.7\%$ ), *tert*-butyl alcohol (TBA,  $\geq 99.7\%$ ) and acetonitrile ( $\geq 99.5\%$ ) were purchased from the Sinopharm Chemical Reagent Co., Ltd. Di-tetrabutylammonium *cis*-bis (isothiocyanato) bis (2,2'-bipyridyl-4,4'-dicarboxylato) ruthenium(II) (N719,  $\geq 99\%$ ), lithium iodide ( $99.9\%$  trace metals basis), iodine ( $\geq 99.99\%$  trace metals basis), 4-*tert*-butyl pyridine (TBP,  $96\%$ ) and surlin polymer frame ( $25 \mu\text{m}$ ) were purchased from Shanghai Aladdin Bio-

Chem Technology Co., Ltd. Gold counter-electrode and deionized water were made in our laboratory. The FTO was washed with acetone, isopropanol and deionized water before use.

### Synthesis of $\text{TiO}_2$ compact layers

Step one: the pure Ti compact layer was sputtered on FTO glass substrate using a magnetron sputter coater.<sup>47</sup> The chamber consisted of a rotating substrate holder with adjustable height and a 50 mm diameter target-base. A water-cooling system was used. The pure Ti compact layer was deposited using a pure Ti target ( $99.995\%$ ) with a high purity Ar ( $99.99\%$ ) at room temperature. The base pressure in the chamber prior to any deposition was  $4 \times 10^{-4} \text{ Pa}$ . For pure Ti compact layer deposition the target-substrate distance was 80 mm, the sputtering power was 125 W, the flow rate of argon was kept at a constant value of 43 sccm, and the sputtering pressure was kept at 0.55 Pa during the deposition. The target was presputtered for 10 min prior to sputtering to remove the oxide layer from the target surface. The sputtering time was varied between 5 and 30 min.

Step two: the pure Ti compact layers were transformed into  $\text{TiO}_2$  compact layers by oxidation treatment. The pure Ti compact layers were sputtered on FTO glass substrate and were placed in a muffle furnace and oxidized at  $550^\circ\text{C}$  for a period of time in a nitrogen-oxygen mixed atmosphere ( $\text{N}_2/\text{O}_2$ , v/v, 4/1). Then, the oxidized compact layers were treated in a 50 mM  $\text{TiCl}_4$  aqueous solution at  $80^\circ\text{C}$  for a period of time, and washed with deionized water to obtain  $\text{TCL}_5$ ,  $\text{TCL}_{10}$ ,  $\text{TCL}_{20}$  and  $\text{TCL}_{30}$ .

### Synthesis of $\text{TiO}_2$ nanorods array films

A mixed solution of concentrated hydrochloric acid and deionized water (v/v, 1/1, 60 mL) was taken, and then 1 mL tetrabutyl titanate was slowly added to the hydrochloric acid aqueous solution at a rate of about 1 drop per 3 s with continuous vigorous stirring to avoid the hydrolysis of tetrabutyl titanate until the solution was clear and transparent. The prepared  $\text{FTO}_{\text{TCL}}$  was placed in a Teflon liner (50 mL) at an angle of  $45\text{--}60^\circ$  to the vertical wall and the as-prepared solution was poured into the Teflon liner and sealed; then, the reactor was placed at a constant temperature in an oven at  $150^\circ\text{C}$  for the hydrothermal reaction.<sup>48</sup> After that, the  $\text{FTO}_{\text{TCL}}$  was removed and washed several times with absolute ethanol and deionized water, and then the dried  $\text{FTO}_{\text{TCL}}$  was annealed in a muffle furnace at  $450^\circ\text{C}$  for a period of time to obtain the TNA film.

### Fabrication of DSSCs

For the fabrication of DSSCs, TNA film photoanodes were dipped in N719 dye ethanol/TBA (v/v, 1/1) solution ( $5 \times 10^{-4} \text{ M}$ ) for 24 h. Then, the photoanodes were withdrawn from the solution and dried under a stream of argon. A gold counter-electrode and a dye-coated photoanode were, then, put together with the surlin polymer frame and heated at  $110^\circ\text{C}$  to adhere to the electrodes. The electrolyte consisted of 0.05 M  $\text{I}_2$ , 0.5 M LiI and 0.5 M *tert*-butyl pyridine in acetonitrile.



## Characterization

The morphology of the samples was examined by the field-emission scanning electron microscopy (FESEM, JSM-7800 F, JEOL). The X-ray diffraction data was acquired using a Bruker D8 Advance powder X-ray diffractometer (XRD, Bruker) with the X-ray tube producing Cu K $\alpha$  radiation ( $\lambda = 1.5406 \text{ \AA}$ ) and the generator set at 40 kV and 40 mA during data collection. Data was collected from  $20$ – $80^\circ$  ( $2\theta$ ). A UV-visible spectrophotometer (UV-2600, Shimadzu) was utilized to obtain the transmittance spectra and absorption spectra of the TNA films. The photoluminescence (PL) experiments were performed using a WFY-28 Fluorescence spectrophotometer (Tianjin Tuo Pu Instrument Co., Ltd). The EIS, Bode plots and Mott-Schottky plots were

measured by an electrochemical workstation (CHI660D, Beijing Join Technology Co., Ltd) at a bias of  $0.3 \text{ V}$  with the frequency sweeping from  $1 \text{ Hz}$  to  $0.1 \text{ MHz}$ , and the data were fitted using ZSimpWin software. A solar simulator was used for  $I$ - $V$  measurements (AM1.5G,  $100 \text{ mW cm}^{-2}$ , SolarIV, Beijing Zolix Instruments Co., Ltd), which was calibrated by a 91150-KG5 reference cell (Newport, USA). All samples were measured at room temperature.

## Results and discussion

### Morphology and structure

Fig. 1a–d represent the FESEM images of the TNA films grown over different TCLs. It can be seen from the side-views of TNA

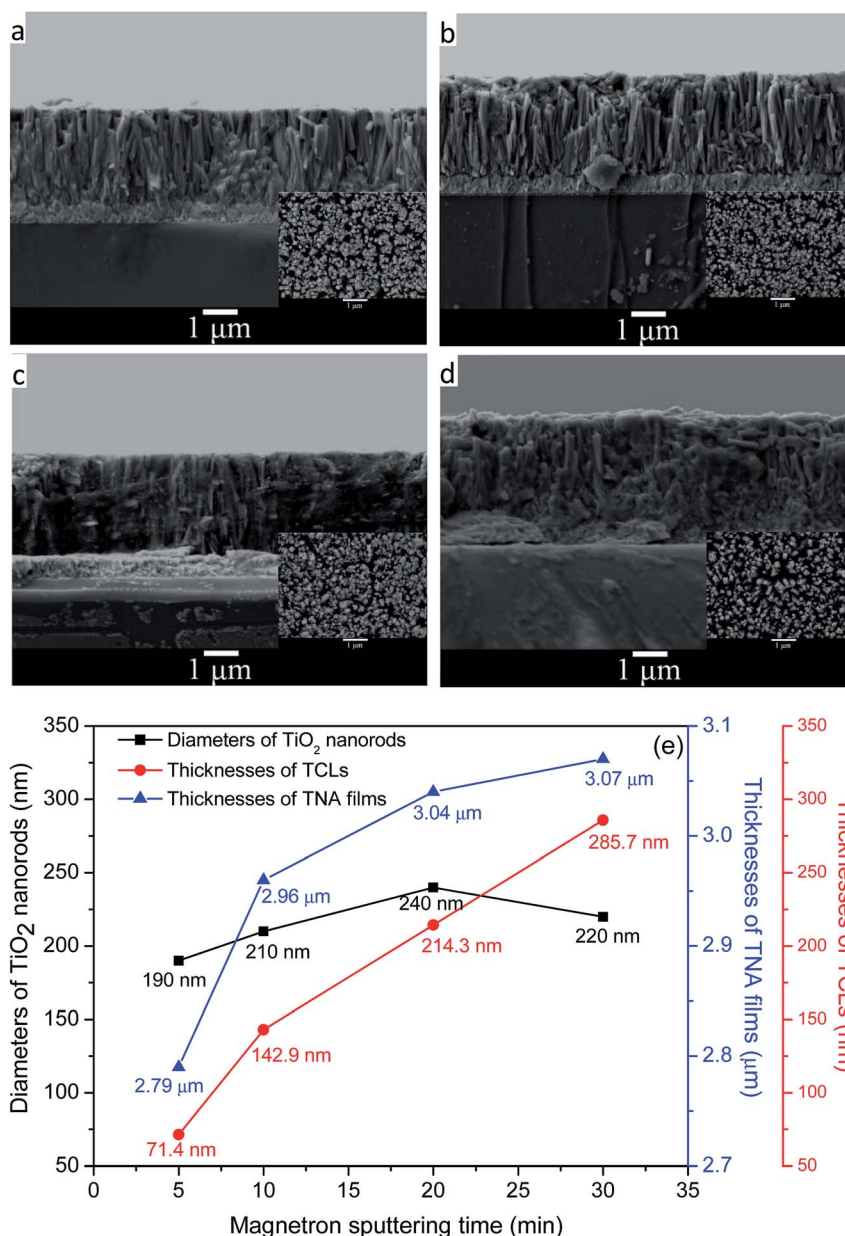


Fig. 1 FESEM images of various TNA films grown over different TCLs: (a) TCL<sub>5</sub>, (b) TCL<sub>10</sub>, (c) TCL<sub>20</sub>, (d) TCL<sub>30</sub>, and (e) the thicknesses of TCLs, thicknesses of TNA films and diameters of TiO<sub>2</sub> nanorods.



films that all TiO<sub>2</sub> nanorods grew perpendicular to the substrate and the bottom end of nanorods is tightly bonded to the substrate; however, the morphology of TiO<sub>2</sub> nanorods is significantly different for different TCLs. The TiO<sub>2</sub> nanorods prepared on TCL<sub>5</sub> and TCL<sub>10</sub> (Fig. 1a and b) are loose and uneven. Moreover, the TiO<sub>2</sub> nanorod fragmentation is serious, which significantly reduces the overall compactness of the TNA films, destroys the array structure of TiO<sub>2</sub> nanorods and results in the increase of crystal defects, namely, interface and surface states, and then impedes the transfer of charge in the TNA films and adversely affects the photoelectric performance of TNA films. However, the TiO<sub>2</sub> nanorods grown over TCL<sub>20</sub> (Fig. 1c) are closely connected with each other, uniform and compact, orderly arranged and without fragmentation, which indicates the good crystal integrity of TiO<sub>2</sub> nanorods and has a positive effect on the reduction of crystal defects in the TNA films. Furthermore, the combined action of dense TNA films and TCL<sub>20</sub> in DSSCs can effectively prevent the direct contact between the conductive layer of FTO and the redox electrolyte to reduce the dark current.<sup>28</sup> In Fig. 1d, the top-view of TiO<sub>2</sub> nanorods grown over TCL<sub>30</sub> shows tetragonal rod-like morphology. However, side-view shows that the TiO<sub>2</sub> nanorods below their middles have fused together and are irregular and fragmented, which can seriously damage the array structure of TNA films and affect their charge transfer performance. In addition, the compactness of TNA films also decreases significantly.

In Fig. 1e, the thicknesses of TNA films increases with the increase in the thicknesses of TCLs, but the rate of increase gradually decreased (6.09%, 2.70%, 0.99%), which indicates that TCLs had a diminishing influence on the thicknesses of the TNA films. The average diameter of TiO<sub>2</sub> nanorods first increases and reaches a maximum (at about 240 nm) with magnetron sputtering for 20 min, and then the diameter decreases. However, the increase in the average diameter of TiO<sub>2</sub> nanorods (10.53%, 14.29%, and -8.33%) is greater than the increase in the thicknesses of the TNA films, indicating that the diameters of TiO<sub>2</sub> nanorods are more susceptible to the TCLs. The increase in the diameter of the TiO<sub>2</sub> nanorods

increases the specific surface area of the TNA films, providing more active surface for the adsorption of the N719 dye, thereby enhancing the absorption of light by the TNA films.

Fig. 2 shows the XRD patterns of TNA films grown over different FTO<sub>TCL</sub>. The XRD patterns of TNA films contain seven peaks, five of which arise from the FTO substrate (JCPDS no. 77-452) and the other two diffraction peaks at 36.22° and 62.91° are assigned to the (101) and (002) planes of tetragonal rutile TiO<sub>2</sub> (JCPDS no 65-192).<sup>49</sup> As can be seen from Fig. 2a, the intensity of the (002) peak of TNA films is significantly enhanced, while the other diffraction peaks of TNA films become weak or even disappear. This is because TCLs can be used as the TiO<sub>2</sub> seed layers to eliminate the lattice mismatch between TiO<sub>2</sub> crystal and FTO substrate, thus, these TiO<sub>2</sub> crystals can grow better over TCLs. The only (002) strong diffraction peak also proves that the TiO<sub>2</sub> nanorods grow in the [001] direction with the growth axis parallel to the substrate surface normal.<sup>27,29</sup> For TCL<sub>5</sub>, TCL<sub>10</sub> and TCL<sub>20</sub>, the intensity of the (002) peak of TNA films gradually increases; however, for TCL<sub>30</sub>, it is the same as that for TCL<sub>20</sub>. This shows that the increasing thickness of TCLs can improve the crystallization performance of TiO<sub>2</sub> to a certain extent and promote the better oriented crystallization growth of TiO<sub>2</sub> nanorods. Fig. 2b demonstrates the partial XRD patterns of (002) peak. When compared with the (002) peak for TCL<sub>5</sub>, the other three (002) peaks shift 0.12° to the small angles (the effects of other error factors have been ruled out), making the 2θ of (002) peak more consistent with the standard tetragonal rutile TiO<sub>2</sub>. This shows that increasing the thickness of TCL can improve the crystal integrity of TiO<sub>2</sub> nanorods and promote the growth of TiO<sub>2</sub> crystals in accordance with the tetragonal rutile TiO<sub>2</sub> lattice arrangement rules. This is because of the lattice mismatch between the TiO<sub>2</sub> crystal and the SnO<sub>2</sub> crystal in the FTO substrate. To eliminate this mismatch, a TiO<sub>2</sub> pre-fabricated layer should be deposited between the TiO<sub>2</sub> crystal and the SnO<sub>2</sub> crystal in advance. However, the elimination of lattice mismatch is not an overnight process, but a gradual easing process. Only when the TiO<sub>2</sub> pre-fabricated layer reaches a certain thickness, the lattice mismatch can be gradually alleviated and eliminated, and this TCL is the TiO<sub>2</sub> pre-fabricated

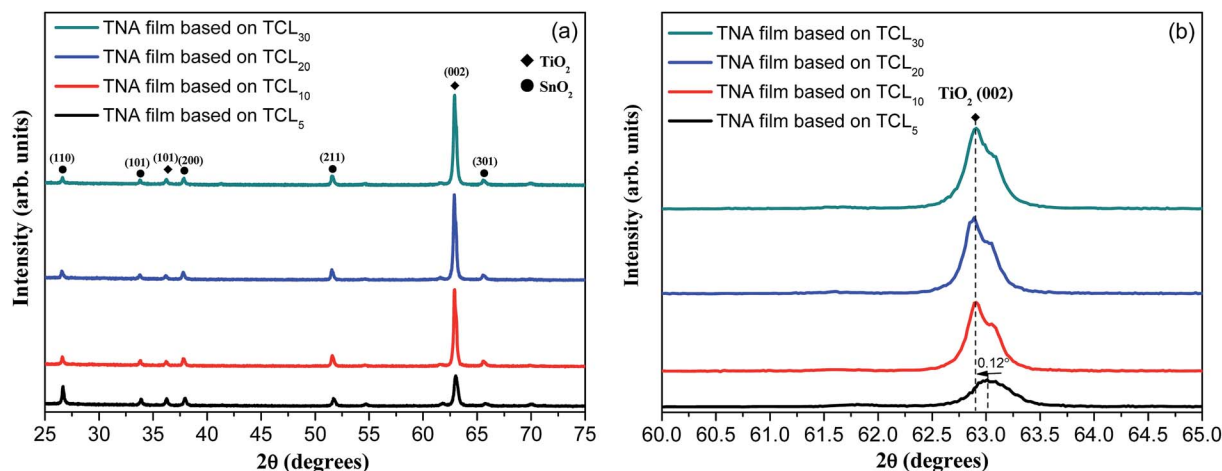


Fig. 2 (a) XRD patterns of various TNA films grown on different TCLs and (b) the XRD patterns of (002) diffraction peak.





layer. Therefore, the maximum intensity of (002) diffraction peak and good morphology (Fig. 1c) of TNA films based on  $\text{TCL}_{20}$  has shown that this TCL thickness (214.3 nm, Fig. 1e) has well eliminated the effect of lattice mismatch for the directional growth of  $\text{TiO}_2$  crystals.

### Optical performance

The UV-Vis spectra of obtained TNA films were characterized as shown in Fig. 3. From Fig. 3a, the light absorption band edges of various TNA films grown over different TCLs are not significantly offset, which indicates that the crystal band-gap structure of  $\text{TiO}_2$  nanorods based on different TCLs has not changed. Moreover, the corresponding band-gaps ( $E_g$ , Fig. 3b) also change very little and are basically consistent with the  $E_g$  (3.03 eV) of the standard tetragonal rutile  $\text{TiO}_2$ . This is because the purpose of this study was to introduce TCLs by the two-step method and to prepare well-crystallized  $\text{TiO}_2$  nanorods. Since both are composed of the same pure  $\text{TiO}_2$  crystal, there is no change in the crystal structure or phase and the light absorption band edges of all TNA films are basically the same. However, the absorbance of TNA films in the ultraviolet region is gradually enhanced with the increase in thicknesses of TCLs. Similarly, as the thickness of TCL increases, the transmittance of TNA films is significantly enhanced in the

visible region, which allows more visible light through the TNA films for energy conversion in the N719 dye layers. This is mainly attributed to the fact that TCLs with certain thickness eliminate the lattice mismatch and promote the crystal integrity of  $\text{TiO}_2$  nanorod crystals, which reduces the morphological and structural defects of  $\text{TiO}_2$  nanorods and makes the  $\text{TiO}_2$  nanorod array more orderly, reducing the scattering of TNA films under visible light and allowing more visible light through TNA films to reach the light absorption layers.

The photoluminescence spectra are commonly used to characterize electronic structures and electronic states in semiconductor materials. In Fig. 3d (the excitation wavelength is 260 nm), the shape of the PL spectrum of all TNA films is basically similar, which indicates that the energy level distribution of  $\text{TiO}_2$  crystals in all TNA films has no obvious change, and the distribution of the electronic state density of  $\text{TiO}_2$  crystals in the band-gaps is also basically similar.<sup>50</sup> As shown in Fig. 3d, with the increase of TCL thickness, the PL intensity of TNA films decreases significantly, and the PL intensity of the TNA film based on  $\text{TCL}_{20}$  reaches the lowest value. This change is also attributed to the improvement in the crystallization performance of  $\text{TiO}_2$  nanorods caused by TCLs. The appropriate thicknesses of TCLs can improve the  $\text{TiO}_2$  crystal integrity, thus

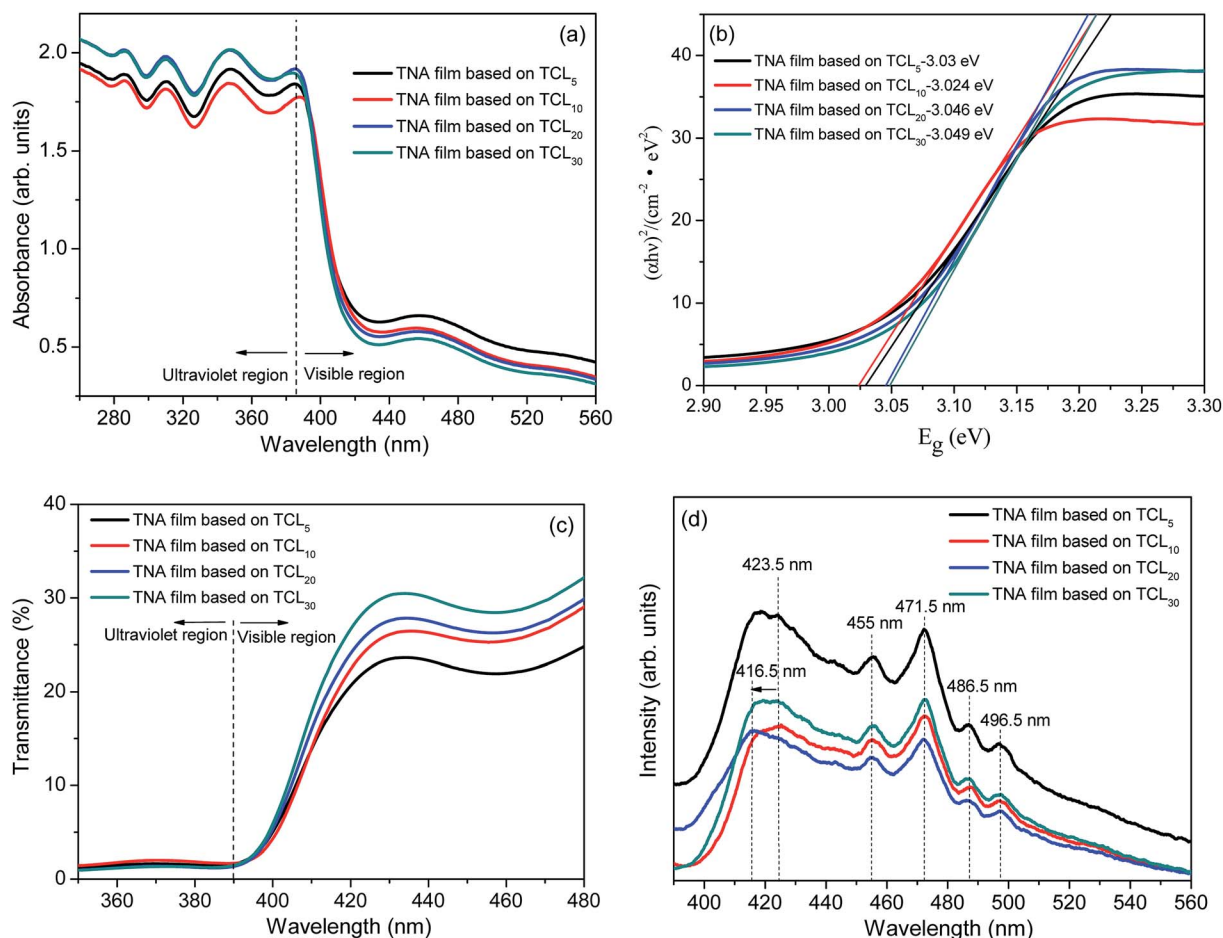


Fig. 3 (a) Absorption spectrum, (b)  $E_g - (\alpha h\nu)^2$  plots, (c) transmittance spectrum, and (d) PL spectrum of various TNA films grown over different TCLs.



reducing the defect concentration in  $\text{TiO}_2$  crystals,<sup>51</sup> which in turn reduces the charge recombination center caused by the defect, effectively separating the photogenerated electrons and holes. Since the charge recombination rate is lowered, the intensity of fluorescence generated by charge recombination is also lowered. Therefore, the maximum intensity of the (002) diffraction peak (Fig. 2a) and good morphology (Fig. 1c) of TNA films grown over  $\text{TCL}_{20}$  show that the lowest PL strength benefits from the well-crystallized  $\text{TiO}_2$  nanorod crystal. In addition, according to the position and intensity analysis of the PL peaks, the PL peak at 423.5 nm is the bound exciton peak with weak intensity, and the PL peak at 455 nm is its phonon peak. The sharp PL peak at 471.5 nm is a free exciton peak with strong intensity, and the latter two PL peaks at 486.5 nm and 496.5 nm are their phonon peaks.<sup>52</sup> However, the blue shift of the bound exciton peak of TNA films grown over  $\text{TCL}_{20}$  from 423.5 nm to 416.5 nm is due to the crystal integrity of the  $\text{TiO}_2$

nanorods, which makes it difficult for photons with a wavelength of 423.5 nm to excite the bound exciton in the  $\text{TiO}_2$  crystals. When the photon wavelength blue shifts to 416.5 nm, the bound exciton absorbs the photon and is excited, and then generates the corresponding PL peak when it transitions back to the ground state.

### Electrical performance

EIS was employed to investigate the charge transfer processes at various interfaces.<sup>53,54</sup> Frequency sweeping test from 1 Hz to 0.1 MHz at a bias voltage of 0.3 V was applied. A 0.5 M  $\text{Na}_2\text{SO}_4$  solution was used as the electrolyte, while platinum electrode, and saturated calomel electrode were used as the counter and reference electrodes, respectively. Fig. 4a presents the Nyquist plots of various TNA films grown over different TCLs. In the fitting circuit,  $R_s$ ,  $R_{ct}$ ,  $R_{ic}$  and  $R_{rec}$  are the liquid–solid interface

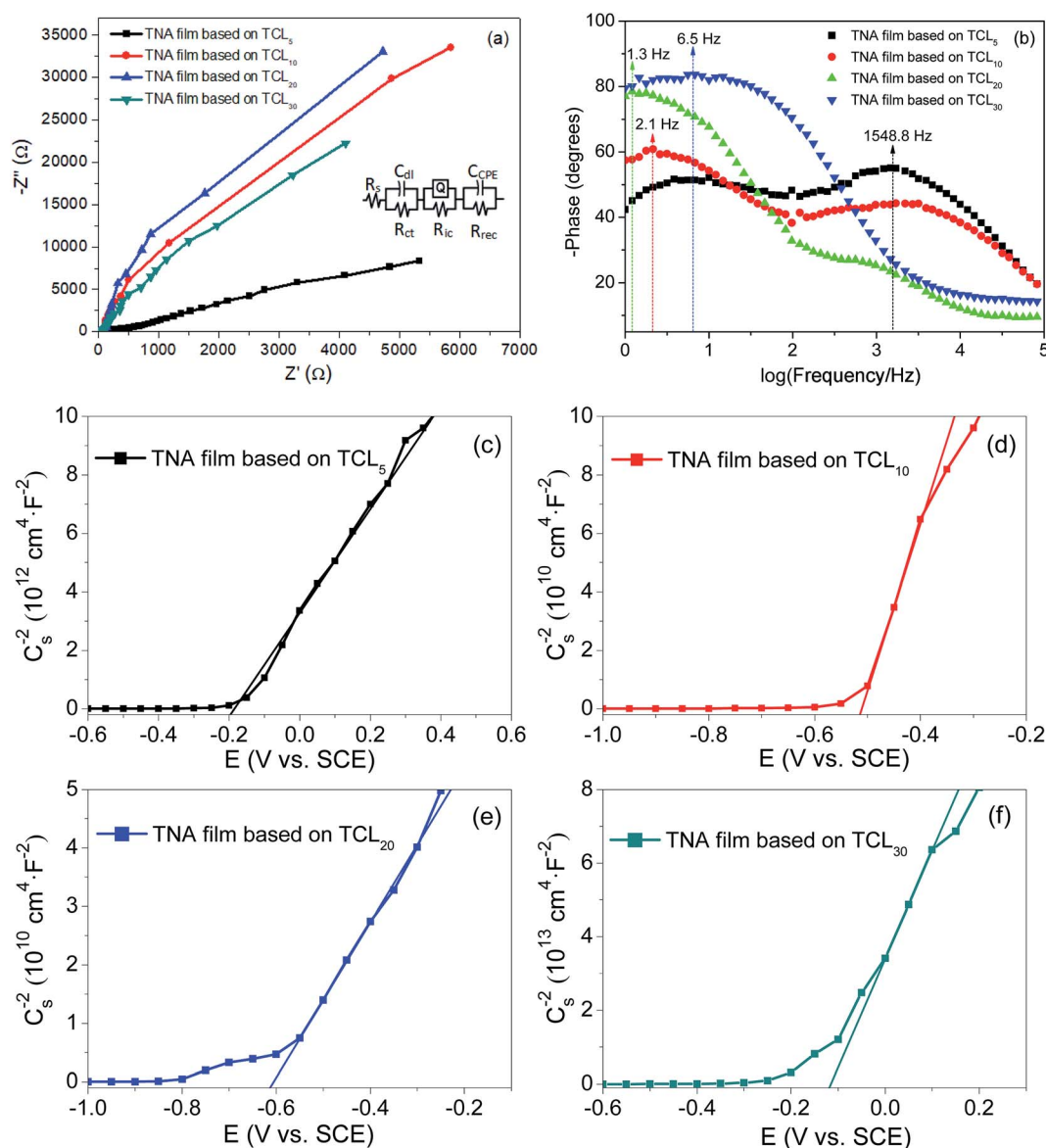


Fig. 4 (a) Nyquist plots, (b) Bode plots, and (c)–(f) Mott–Schottky plots of various TNA films grown over different TCLs.



Table 1 Fitting results of the Nyquist plots

TNA films grown over	$R_s$ ( $\Omega$ )	$R_{ct}$ ( $\Omega$ )	$R_{ic}$ (k $\Omega$ )	$R_{rec}$ (k $\Omega$ )	$Y_0$ ( $10^{-5} \Omega^{-1} \text{cm}^{-2} \text{s}^n$ )	$n$
TCL <sub>5</sub>	9.4	370.9	0.4	860	1.5	0.71
TCL <sub>10</sub>	12.2	53.1	2800	1500	5.4	0.75
TCL <sub>20</sub>	6.7	22.7	280	4600	4.6	0.85
TCL <sub>30</sub>	5.6	32.9	39	3700	3.1	0.26

resistance between the active electrode and electrolyte, charge transfer resistance, solid–solid interface resistance between TNA films and FTO substrate and charge recombination resistance, respectively. The fitting results of the Nyquist plots are shown in Table 1. According to the fitting results, the  $R_s$ ,  $R_{ct}$  and  $R_{ic}$  of TNA films decrease significantly with the increase in the TCL thickness, which indicates that the charge transfer performance in different interfaces and thin films has been effectively improved, and the increase in  $R_{rec}$  further inhibits the charge recombination process. With the improvement in the charge transfer process and the reduction of charge recombination, the effective charge collection rate is improved, which lays a foundation for improving the current density of DSSCs. The  $R_{ct}$  and  $R_{rec}$  of the TNA film grown over TCL<sub>20</sub> achieve a minimum (22.7  $\Omega$ ) and a maximum (4600 k $\Omega$ ), indicating that this TNA film has a relatively better charge transfer performance. As the constant phase element (CPE), admittance ( $Y_0$ ) characterizes the conductivity of the film, and the larger the  $Y_0$ , the better the conductivity. Moreover,  $n$  represents the physical properties of the element, which to some extent can represent the roughness or porosity of the film surface. The closer  $n$  is to 1, the smoother the film surface and the smaller the porosity. In Table 1,  $Y_0$  and  $n$  increase with the increase in the TCL thickness (from TCL<sub>5</sub> to TCL<sub>20</sub>), following which the  $Y_0$  and  $n$  of TNA films grown over TCL<sub>30</sub> reduce. It is shown that the TCL of appropriate thickness can significantly improve the conductivity and reduce the porosity of TNA films. Thus, the TNA film based on TCL<sub>20</sub> not only has good conductivity but also has the smallest porosity, also confirming the observed better morphology in Fig. 1c.

Fig. 4b shows the representative Bode plots of TNA films grown over different TCLs. The frequency peak is related to the electron transfer processes at various interfaces, and the electron lifetime ( $\tau_e$ , Table 2) can be estimated from the Bode plots via the following equation:<sup>32</sup>

$$\tau_e = \frac{1}{2\pi f_{\max}} \quad (1)$$

where  $f_{\max}$  is the maximum frequency from Bode plots.

The results show that the increase in the TCL thickness greatly prolongs the electron lifetime, and  $\tau_e$  of TNA film grown over TCL<sub>20</sub> is as high as 122.43 ms. The higher electron lifetime means less charge recombination. Thus, this result reveals that the TCLs increase in thickness; especially, TCL<sub>20</sub> promotes the charge separation, and then increases the conductivity of TNA films. In Fig. 4b, it also can be noted that the change in TCL thickness induces a shift of phase angle to lower frequency. This

may be attributed to the fast transport and collection of the charge in the TNA films.

Fig. 4c–f display the Mott–Schottky plots of various TNA films grown over different TCLs. According to the positive slopes, it is known that all TNA films have n-type semiconductor behavior. Accordingly, the flat-band potential ( $E_{fb}$ ) and donor density ( $N_D$ ) of TNA films can be derived from the Mott–Schottky plots in terms of the Mott–Schottky equation:<sup>55–57</sup>

$$\frac{1}{C_s^2} = \frac{2}{e\epsilon\epsilon_0 N_D} \left( E - E_{fb} - \frac{k_B T}{e} \right) \quad (2)$$

where  $C_s$  is the capacitance of the space charge region,  $e$  is the electronic charge ( $1.6 \times 10^{-19}$  C),  $\epsilon$  is the relative dielectric constant (180) and  $\epsilon_0$  is the vacuum permittivity ( $8.86 \times 10^{-14}$  F cm<sup>-1</sup>),  $N_D$  is the donor density,  $E$  is the applied potential and  $E_{fb}$  is the flat-band potential,  $k_B$  is the Boltzmann constant ( $1.381 \times 10^{-23}$  J K<sup>-1</sup>), and  $T$  is the absolute temperature.

The calculated results including the  $N_D$  and  $E_{fb}$  are shown in Table 2. The  $N_D$  of TNA films based on different TCLs increases first and then decreases, and the  $N_D$  of TNA films based on TCL<sub>20</sub> is as high as  $5.91 \times 10^{18} \text{cm}^{-3}$ . The higher  $N_D$  means more charge separation, less charge recombination, increased charge collection rate and longer electron lifetime. These changes are attributed to the fact that TCLs with appropriate thickness promote the crystal integrity of TiO<sub>2</sub> nanorods crystals. Well-crystallized TiO<sub>2</sub> crystals improve the morphological structure of TNA films, reduce the crystal defect concentration in TNA films, and thus improve the electrical performance such as charge separation and collection in TNA films. Similarly, the most negative  $E_{fb}$  of TNA films based on TCL<sub>20</sub> is  $-0.62$  V (vs. SCE), and the more negative  $E_{fb}$  means that the quasi-Fermi level of TNA films is closer to the bottom of the conduction band, which improves the  $V_{oc}$  of DSSCs.

### Photovoltaic performance

Fig. 5 shows the  $I$ – $V$  curves and output power density ( $P_{out}$ ) curves of DSSCs measured under an irradiance of  $100 \text{mW cm}^{-2}$

Table 2 Calculated electronic parameters from Bode plots and Mott–Schottky plots

TNA films grown over	$E_{fb}$ (V vs. SCE)	$N_D$ (cm <sup>-3</sup> )	$\tau_e$ (ms)
TCL <sub>5</sub>	−0.19	$4.42 \times 10^{16}$	0.11
TCL <sub>10</sub>	−0.51	$1.38 \times 10^{18}$	75.79
TCL <sub>20</sub>	−0.62	$5.91 \times 10^{18}$	122.43
TCL <sub>30</sub>	−0.12	$2.66 \times 10^{15}$	24.49



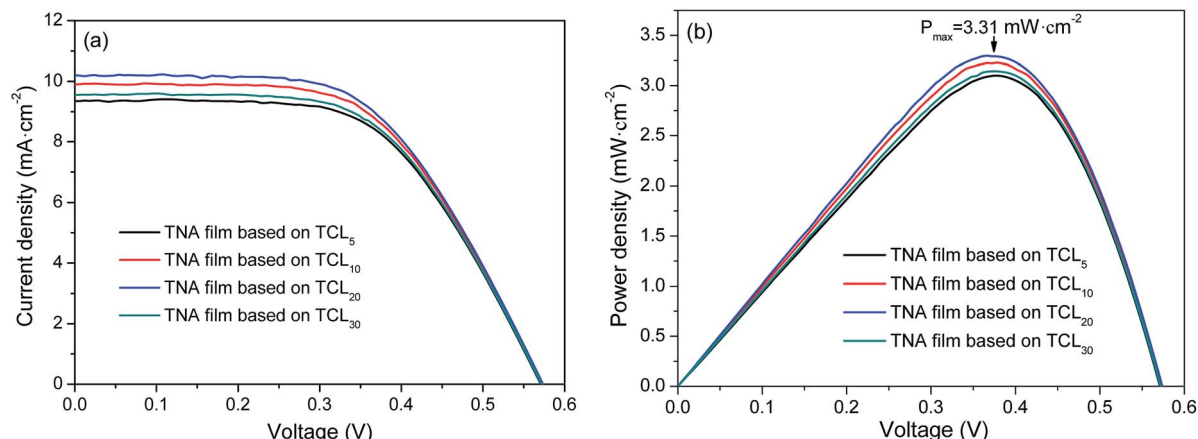


Fig. 5 (a)  $I$ - $V$  curves and (b)  $P_{\text{out}}$  curves of DSSCs grown over various TNA films with different TCLs.

Table 3 Photovoltaic performance parameters of DSSCs

TNA films grown over	$J_{\text{sc}}$ ( $\text{mA cm}^{-2}$ )	$V_{\text{oc}}$ (V)	FF (%)	PCE (%)
TCL <sub>5</sub>	9.3497	0.5711	58.08	3.10
TCL <sub>10</sub>	9.8996	0.5731	56.90	3.23
TCL <sub>20</sub>	10.2054	0.5737	56.30	3.30
TCL <sub>30</sub>	9.5480	0.5716	57.59	3.14

simulated AM1.5G sunlight, and the parameters of DSSCs are summarized in Table 3. As shown in Fig. 5a and Table 3, the TCL thickness shows an obvious influence on the photovoltaic performance of DSSCs. It is seen that with the increased thickness of TCL, the  $V_{\text{oc}}$  changes little and its maximum value is 0.5737 V (based on TCL<sub>20</sub>). The  $J_{\text{sc}}$  increases and in the TNA films based on TCL<sub>20</sub> has an optimized value (10.2054  $\text{mA cm}^{-2}$ ). Although the TNA films grown over TCL<sub>20</sub> achieves a lower FF (56.3%), which still results in the maximum PCE (3.3%). Meanwhile, the TNA film grown over TCL<sub>20</sub> also obtains the maximum  $P_{\text{out}}$  (3.31  $\text{mW cm}^{-2}$ , Fig. 5b). These results indicate that the TNA film grown over TCL<sub>20</sub> present an excellent photovoltaic performance when compared with other TNA films. These results also confirm the above analysis conclusion, among all TNA films grown over different TCLs, the TNA film grown over TCL<sub>20</sub> has the most ideal and comprehensive photoelectrochemical performance.

## Conclusions

This study provides a new method for the preparation of TCLs, which allows the preparation of TCLs more quickly, efficiently, simply and cheaply. The influence of TCL with different thickness on the performance of TNA films also provides a reference for further research. The innovative two-step method was used to prepare perfect TCLs with different thicknesses. Then, the TNA films were successfully grown over the TCLs. The results indicated that TCLs with appropriate thickness could effectively improve the morphology and photoelectric properties of TNA

films. When compared with other TNA films grown over different TCLs, the one grown over TCL<sub>20</sub> exhibited more ideal and comprehensive photoelectrochemical performance. The DSSC based on this TNA film achieved the highest  $J_{\text{sc}}$  (10.2054  $\text{mA cm}^{-2}$ ),  $V_{\text{oc}}$  (0.5737 V), PCE (3.3%) and  $P_{\text{out}}$  (3.31  $\text{mW cm}^{-2}$ ).

## Conflicts of interest

There are no conflicts of interest to declare.

## Acknowledgements

This work was supported by the Chinese Postdoctoral Science Fund (2343/185179), the Chinese 02 Special Fund (2017ZX02408003), the Key Research Projects of Colleges and Universities in Henan Province (15A430023) and the Henan International Science and Technology Cooperation Programs (152102410035).

## References

- 1 M. Saliba, T. Matsui, K. Domanski, J. Y. Seo, A. Ummadisingu, S. M. Zakeeruddin, J. P. C. Baena, W. R. Tress, A. Abate, A. Hagfeldt and M. Grätzel, *Science*, 2016, **354**, 206–209.
- 2 Z. W. Xiao and Y. F. Yan, *Adv. Energy Mater.*, 2017, **7**, 1701136.
- 3 C. Liang, P. W. Li, Y. Q. Zhang, H. Gu, Q. B. Cai, X. T. Liu, J. F. Wang, H. Wen and G. S. Shao, *J. Power Sources*, 2017, **372**, 235–244.
- 4 I. Jeong, H. Jung, M. Park, J. S. Park, H. J. Son, J. Joo, J. Lee and M. J. Ko, *Nano Energy*, 2016, **28**, 380–389.
- 5 Y. M. Xu, X. S. Li, M. Xiao and X. M. Xiong, *CrystEngComm*, 2018, **20**, 6280–6290.
- 6 Q. H. Liu, Q. Sun, M. Zhang, Y. Li, M. Zhao and L. F. Dong, *Appl. Phys. A: Mater. Sci. Process.*, 2016, **122**, 1–5.
- 7 N. Irannejad, B. Rezaei, A. A. Ensafi and M. M. Momeni, *Electrochim. Acta*, 2017, **247**, 764–770.
- 8 M. Asemi and M. Ghanaatshoar, *J. Mater. Sci.*, 2017, **52**, 489–503.





- 9 J. Du, Z. L. Du, J. S. Hu, Z. X. Pan, Q. Shen, J. K. Sun, D. H. Long, H. Dong, L. T. Sun, X. H. Zhong and L. J. Wan, *J. Am. Chem. Soc.*, 2016, **138**, 4201–4209.
- 10 M. X. Liu, O. Voznyy, R. Sabatini, F. P. García de Arquer, R. Munir, A. H. Balawi, X. Z. Lan, F. J. Fan, G. Walters, A. R. Kirmani, S. Hoogland, F. Laquai, A. Amassian and E. H. Sargent, *Nat. Mater.*, 2017, **16**, 258–263.
- 11 W. Wang, W. L. Feng, J. Du, W. N. Xue, L. L. Zhang, L. L. Zhao, Y. Li and X. H. Zhong, *Adv. Mater.*, 2018, 1705746.
- 12 E. M. Sanehira, A. R. Marshall, J. A. Christians, S. P. Harvey, P. N. Ciesielski, L. M. Wheeler, P. Schulz, L. Y. Lin, M. C. Beard and J. M. Luther, *Sci. Adv.*, 2017, **3**, eaao4204.
- 13 W. Chen, M. Liu, Y. H. Wang, L. Gao, H. F. Dang and L. Q. Mao, *Mater. Res. Bull.*, 2019, **116**, 16–21.
- 14 L. Ge, Q. Hong, H. Li and F. Li, *Chem. Commun.*, 2019, **55**, 4945–4948.
- 15 R. K. Sonker, S. Sikarwar, S. R. Sabhajeet, Rahul and B. C. Yadav, *Opt. Mater.*, 2018, **83**, 342–347.
- 16 P. Sanjay, K. Deepa, J. Madhavan and S. Senthil, *Opt. Mater.*, 2018, **83**, 192–199.
- 17 Y. F. Wang, Q. P. Luo, Y. Ding, X. Wang, X. F. Li and D. J. Li, *Mater. Chem. Phys.*, 2018, **207**, 141–146.
- 18 A. Ashok, S. N. Vijayaraghavan, G. E. Unni, S. V. Nair and M. Shanmugam, *Nanotechnology*, 2018, **29**, 175401.
- 19 Y. C. Chen, Y. C. Chang and C. M. Chen, *J. Electrochem. Soc.*, 2018, **165**, F409–F416.
- 20 A. Latini and R. Panetta, *Energies*, 2018, **11**, 975.
- 21 M. Amini, R. Keshavarzi, V. Mirkhani, M. Moghadam, S. Tangestaninejad, I. M. Baltork and F. Sadegh, *J. Mater. Chem. A*, 2018, **6**, 2632–2642.
- 22 J. A. Peñafiel-Castro, B. Hahn, R. L. Maltez, G. Knörnschild, P. Allongue and L. F. P. Dick, *Chem. Commun.*, 2018, **54**, 3251–3254.
- 23 P. Soundarrajan, K. Sankarasubramanian, K. Sethuraman and K. Ramamurthi, *CrystEngComm*, 2014, **16**, 8756–8768.
- 24 X. X. Wang, Y. D. Xiao, D. W. Zeng and C. S. Xie, *CrystEngComm*, 2015, **17**, 1151–1158.
- 25 Y. Y. Li, J. G. Wang, H. H. Sun and B. Q. Wei, *ACS Appl. Mater. Interfaces*, 2018, **10**, 11580–11586.
- 26 P. Leidich, O. Linker, M. Panthöfer and W. Tremel, *CrystEngComm*, 2014, **16**, 8486–8491.
- 27 R. Sivakumar, J. Ramkumar, S. Shaji and M. Paulraj, *Thin Solid Films*, 2016, **615**, 171–176.
- 28 R. Govindaraj, N. Santhosh, M. S. Pandian and P. Ramasamy, *J. Cryst. Growth*, 2017, **468**, 125–128.
- 29 B. B. Çirak, S. M. Karadeniz, T. Kılınc, B. Caglar, A. E. Ekinci, H. Yelgin, M. Kürekçi and Ç. Çirak, *Vacuum*, 2017, **144**, 183–189.
- 30 N. Nyein, W. K. Tan, G. Kawamura, A. Matsuda and Z. Lockman, *J. Photochem. Photobiol., A*, 2017, **343**, 33–39.
- 31 L. Q. Mao, Q. Q. Ba, S. Liu, X. J. Jia, H. Liu, W. Chen and X. Y. Li, *RSC Adv.*, 2018, **8**, 31529–31537.
- 32 Y. L. Wan, M. M. Han, L. M. Yu, G. W. Yi and J. H. Jia, *CrystEngComm*, 2016, **18**, 1577–1584.
- 33 Q. Q. Gao, X. Y. Zhang, L. F. Duan, X. J. Li, X. S. Li, Y. Yang, Q. Yu and W. Lü, *J. Alloys Compd.*, 2017, **715**, 337–343.
- 34 S. S. Kim, S. I. Na and Y. C. Nah, *Electrochim. Acta*, 2011, **58**, 503–509.
- 35 J. Liu, J. Huo, M. Zhang and X. D. Dong, *Thin Solid Films*, 2017, **623**, 25–30.
- 36 S. M. Mokhtar, M. K. Ahmad, C. F. Soon, N. Nafarizal, A. B. Faridah, A. B. Suriani, M. H. Mamat, M. Shimomura and K. Murakami, *Optik*, 2018, **154**, 510–515.
- 37 D. L. Jiang, Y. Q. Hao, R. J. Shen, S. Ghazarian, A. Ramos and F. M. Zhou, *ACS Appl. Mater. Interfaces*, 2013, **5**, 11906–11912.
- 38 I. Jeong, Y. H. Park, S. Bae, M. Park, H. Jeong, P. Lee and M. J. Ko, *ACS Appl. Mater. Interfaces*, 2017, **9**, 36865–36874.
- 39 J. Q. Qin, Z. L. Zhang, W. J. Shi, Y. F. Liu, H. P. Gao and Y. L. Mao, *Nanoscale Res. Lett.*, 2017, **12**, 640.
- 40 R. L. Coppo, B. H. Farnum, B. D. Sherman, N. Y. M. Iha and T. J. Meyer, *Sustainable Energy Fuels*, 2017, **1**, 112–118.
- 41 J. J. Huang, C. K. Wu and C. F. Hsu, *Appl. Phys. A*, 2017, **123**, 741.
- 42 H. J. Liu, H. Bala, B. Zhang, B. B. Zong, L. W. Huang, W. Y. Fu, G. Sun, J. L. Cao and Z. Y. Zhan, *J. Alloys Compd.*, 2018, **736**, 87–92.
- 43 V. Manthina and A. G. Agrios, *Thin Solid Films*, 2016, **598**, 54–59.
- 44 A. E. Shalan, S. Narra, T. Oshikiri, K. Ueno, X. Shi, H. P. Wu, M. M. Elshanawany, E. W. G. Diao and H. Misawa, *Sustainable Energy Fuels*, 2017, **1**, 1533–1540.
- 45 P. Lellig, M. A. Niedermeier, M. Rawolle, M. Meister, F. Laquai, P. M. Buschbaum and J. S. Gutmann, *Phys. Chem. Chem. Phys.*, 2012, **14**, 1607–1613.
- 46 Tanvi, V. Saxena, A. Singh, O. Prakash, A. Mahajan, A. K. Debnath, K. P. Muthe and S. C. Gadkari, *Sol. Energy Mater. Sol. Cells*, 2017, **170**, 127–136.
- 47 G. D. Rajmohan, F. Z. Huang, R. d'Agostino, J. d. Plessis and X. J. Dai, *Thin Solid Films*, 2017, **636**, 307–313.
- 48 B. Liu and E. S. Aydil, *J. Am. Chem. Soc.*, 2009, **131**, 3985–3990.
- 49 Y. F. Deng, Z. H. Ma, F. Z. Ren, G. X. Wang and A. A. Volinsky, *Chem. Phys. Lett.*, 2019, **724**, 42–49.
- 50 W. L. Xu, H. Yuan, J. Xiao, C. Xiong and X. F. Zhu, *Int. J. Mod. Phys. B*, 2017, **31**, 1744053.
- 51 P. Vivo, A. Ojanpera, J. H. Smått, S. Sanden, S. G. Hashmi, K. Kaunisto, P. Ihalainen, M. T. Masood, R. Osterbacka, P. D. Lund and H. Lemmetyinen, *Org. Electron.*, 2017, **41**, 287–293.
- 52 M. A. Alvi, A. A. Alghamdi and M. Zulfequar, *J. Nanoelectron. Optoelectron.*, 2016, **11**, 656–661.
- 53 D. T. Liu, S. B. Li, P. Zhang, Y. F. Wang, R. Zhang, H. Sarvari, F. Wang, J. Wu, Z. M. Wang and Z. D. Chen, *Nano Energy*, 2017, **31**, 462–468.
- 54 J. B. Naceur, R. Ouertani, W. Chakhari and R. Chtourou, *J. Mater. Sci.: Mater. Electron.*, 2019, **30**, 5631–5639.
- 55 A. W. Bott, *Curr. Sep.*, 1998, **17**(3), 87–91.
- 56 X. Y. Niu, W. J. Yan, C. C. Shao, H. L. Zhao and J. K. Yang, *Appl. Surf. Sci.*, 2019, **466**, 882–892.
- 57 K. Chen, C. L. Chen, X. M. Ren, A. Alsaedi and T. Hayat, *Chem. Eng. J.*, 2019, **359**, 944–954.

